

High Fidelity Ladar Simulation

Rastislav Telgarsky, Michael C. Cates, Carolyn Thompson, John N. Sanders-Reed*

ABSTRACT

The ability to extract target features from a ladar Range Resolved Doppler Image (RRDI) can enable target detection, identification, discrimination, and status assessment. Extraction of these features depends on the image processing algorithms, target characteristics, and image quality. The latter in turn depends on ladar transmitter and receiver characteristics, propagation effects, target/beam interactions, and receiver signal processing. In order to develop hardware systems and processing algorithms for a specific application, it is necessary to understand how these factors interact. A modular, high fidelity ladar simulation has been developed which provides modeling of each step from transmitter, through feature extraction.

Keywords: ladar, simulation, Range-Resolved, Doppler, RRDI, laser radar, heterodyne, BRDF

1. INTRODUCTION

A high fidelity ladar simulation has been developed to support ladar hardware device development and to support system engineering studies to understand how ladar devices can improve mission effectiveness. The key attributes of this ladar simulation are that 1) It is modular, allowing great variation in design parameters, such as pulse shapes and spacing, power, optics, wavefront propagation, target interaction, and signal processing; 2) It supports arbitrary target types through the use of solid CAD models and propagators for target motion; 3) The primary focus is on Range Resolved Doppler Imaging (RRDI). Particular attention is paid to the radiometry of the simulation, including basic geometric factors (optics size, power, and range to target), target interactions, detector effects, and signal processing required to form the RRD image. In addition, elementary image processing algorithms have been developed to extract generic RRDI features such as range length, Doppler width, and total intensity of targets. Further work has been done to describe how these features evolve over time.

With this simulation it is possible to investigate how RRD image quality varies as a function of ladar device parameters, sensor to target geometry, and signal processing algorithms. It is also possible to investigate how various image processing and feature extraction algorithms perform as a function of image quality, and hence it is possible to investigate feature extraction and discrimination as a function of various device and target geometry factors. This in turn allows optimization of the ladar device design for various applications.

Another feature of the simulation code is the ability to adjust the fidelity of the RRD image generation, from high fidelity with all of the various effects included, to a much simpler simulation which produces essentially noise free images. These noise free images can be useful for visualizing what an RRD image would look like for complex shaped objects. This quick visualization can be used to develop algorithm concepts, prior to running the more time consuming high fidelity image generation.

2. SIMULATION

2.1. Overview

Laser Radar or ladar can be thought of as a standard microwave radar [1], operating at a much shorter wavelength. This means that while the same basic principles and equations apply, a number of phenomena, including beam propagation and target interactions, will change substantially. The ladar range equation [2] relates optical power at the receiver (P_R) to transmitted power (P_T), a beam shape parameter (K), the beam width ϕ (in radians), range to target (R), target surface

*Boeing-SVS, Inc. 4411 The 25 Way NE, Albuquerque, NM 87109

area (A), a material and viewing angle specific reflectivity factor (B), attenuation factors for outgoing transmission, and return reflection propagation (η_T, η_R), and the diameter of the receiver aperture (D):

$$P_R = P_T \left(\frac{16K}{\phi^2} \right) \left(\frac{\eta_T}{4\pi R^2} \right) (A * B) \left(\frac{\eta_R}{4\pi R^2} \right) \left(\frac{\pi D^2}{4} \right) \quad (1)$$

The exact form of this equation depends on definitions of some of the parameters. For example, the reflectivity (B) in the above equation includes the surface orientation, so the area is the target surface area, not the projected area. Similarly, the reflectivity is defined to include reflection into 4π steradians.

Many of these factors have a strong wavelength dependence, resulting in not only quantitative, but often qualitative differences from radio frequency radar. These phenomena must be accurately modeled to produce a high fidelity simulation. In particular, since we model heterodyne detection techniques for RRD imaging, phase related phenomenon introduced during beam propagation and target interaction can become dominant effects which must be properly modeled in order to accurately generate RRD images. The rest of this section describes the various modules in the simulation.

The simulation program is written entirely in Matlab and consists of several modules passing the data from one to the next by files. Each of the modules is menu driven with the ability to save parameters to configuration files. We handle accurately a variety of ladar configurations with the correct radiometric parameters. In the first module we set-up the target shape, target dynamics, pulse shape and other ladar parameters to see the effects in various visualization tools and performance measures. The table in figure 1 shows the main functions of the modules.

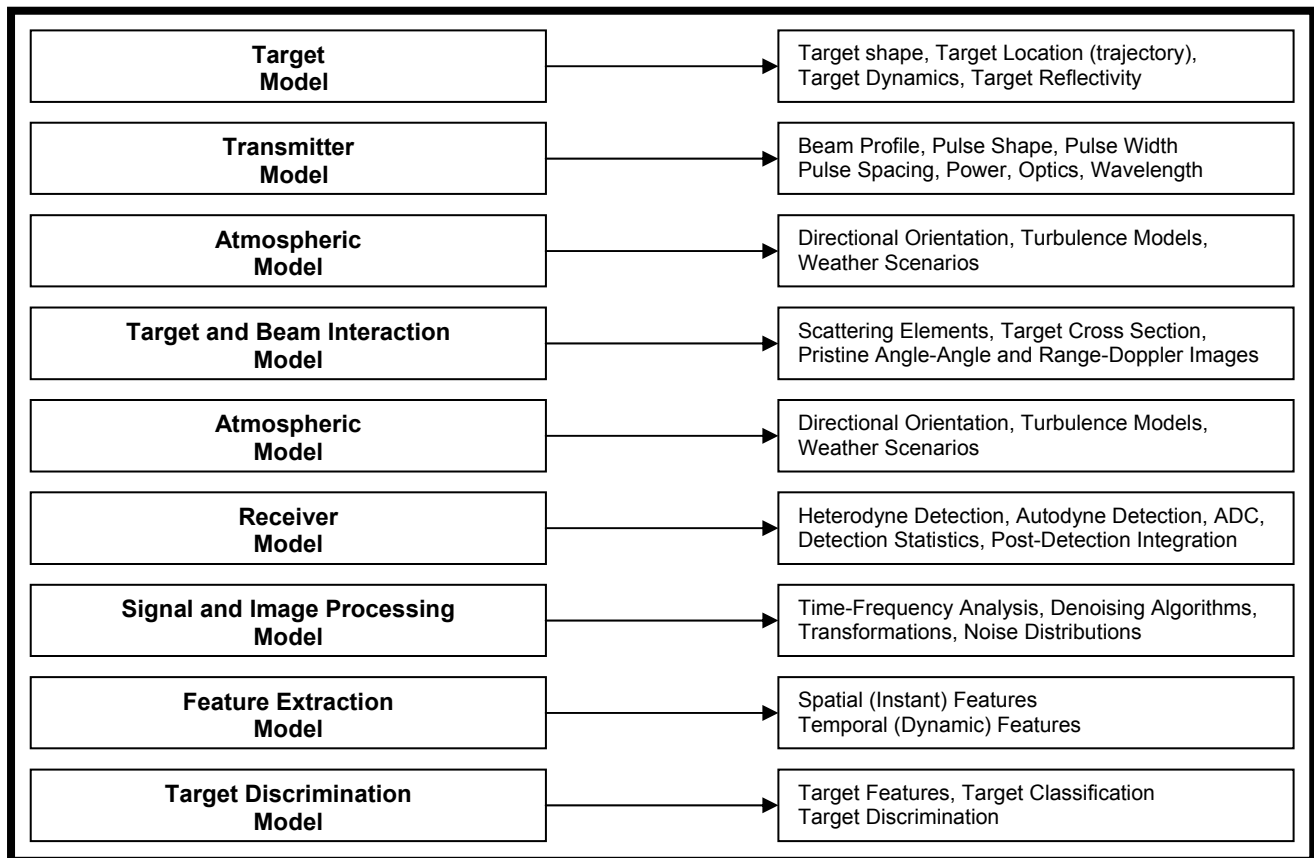


Figure 1. Main simulation processing modules

Each model contains options that are selectable from menus or loaded from a configuration file. The target model contains options for target structure (shape, materials) and dynamics (trajectory and orientation). The transmitter model contains options for pulse width, pulse spacing, pulse shape, number of pulses, laser wavelength, beam profile and aperture diameter. The receiver model contains options for sampling rate, intermediate frequencies, target distance, receiver diameter, and various efficiency factors. In addition, there are ancillary options such as: number of range-Doppler images to be summed for a Post-Detection Integration (PDI), detection type, and type of signal processing to be performed. The following sections describe the individual modules.

The current simulation models the RRD image formation and processing functions but does not model system level aspects such as search, target acquisition, and revisit sampling. These have been investigated under separate efforts.

2.2. Transmitter

The transmitter model allows us to define the optical wavelength, the temporal and spatial characteristics of the pulses, the transmitter aperture shape, and the pulse energy. We define spatial and temporal beam shapes in terms of the electric field amplitude. Observed intensity profiles will $|E|^2$ will tend to be different, depending on the profile used.

The temporal sub-system allows us to define the shape and width (T_p) of individual pulses, and the spacing between pulses (T_s). A group of evenly spaced pulses is termed a “macro-pulse” or “burst”. The number of pulses in a macro-pulse (N_p), and the spacing between macro-pulses is also specified. Energy from a single macro-pulse is coherently processed to form a RRD image. Energy from a series of macro-pulses (called a salvo) is incoherently summed to form a Post-Detection Integration (PDI) image (figure 2). A PDI image averages speckle from individual images, thus reducing speckle effects, as well as increasing total received signal.

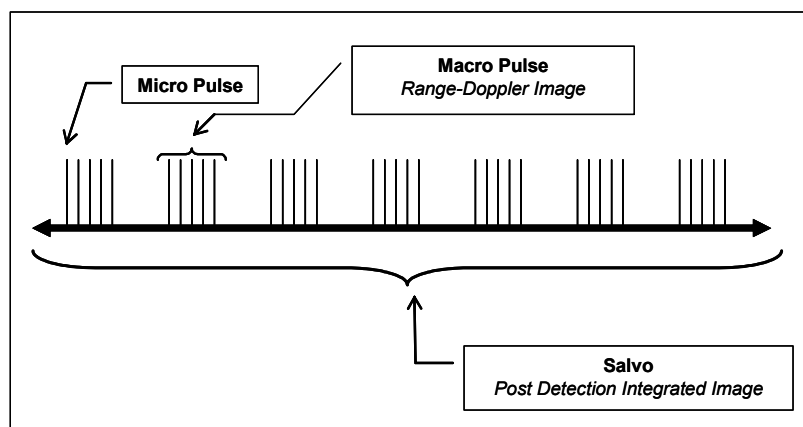


Figure 2. Relationship of pulses, macro-pulses, and salvos to individual RRD images and PDI images.

A macro-pulse or burst is defined using a matrix in which each row represents a single pulse. The temporal amplitude shape of an individual pulse is defined by samples along the row. Various pre-programmed pulse shapes are available, such as Gaussian, rectangular, and saw-tooth, however, other shapes can be easily added. The pulse shape function is sampled at a rate of F_i with N_i samples, for a total pulse window duration N_i/F_i .

The basic device parameters just described are related to the minimum resolvable Doppler shift and range increment, and to the maximum, unambiguous Doppler shift and range extent by a series of simple equations [1-4] shown in figure 3. Velocity is related to Doppler shift as shown in the table. The speed of light (c) and the wavelength of the light (λ) are the remaining parameters. Optimal RRD image sizing is such that each pixel corresponds to the minimum resolvable range or Doppler increment, and the total number of pixels corresponds to the number of bins in the unambiguous extents. The range and velocity extents values are also referred to as range and velocity ambiguities (Jelalian [3]).

The simulation utilizes a target plane spatial amplitude distribution matrix for the far field illumination pattern. The simulation models a Gaussian beam profile and circular output aperture, which results in an Airy like distribution in the far field. If the beam profile is small compared to the aperture diameter, the far field distribution is predominantly Gaussian, while if the beam profile is large compared to the aperture diameter, resulting in a clipped Gaussian, the far field will have a strong Airy characteristic [5]. Alternatively, an externally supplied amplitude distribution may be used.

	Minimum Increment	Unambiguous Extent	Number of bins
Sample Time	$\frac{1}{F_i}$	$T_s * N_p$	$(T_s * N_p) * F_i$
Range	$\frac{c * T_p}{2}$	$\frac{c * T_s}{2}$	$\frac{T_s}{T_p}$
Doppler Frequency	$\frac{1}{T_s * N_p}$	$\frac{1}{T_s}$	N_p
Doppler Velocity	$\frac{\lambda}{2(T_s * N_p)}$	$\frac{\lambda}{2(T_s)}$	N_p

Figure 3. Relation of device parameters to observables.

The transmitter produces the incident wave (E-field) illuminating the target. While we think about this wave as having the frequency of light at the wavelength λ , we use much slower sampling rate F_i (on the order of $1/T_p$) to represent it in digital processing of incident and reflected waves.

2.3. Propagation

The simulation has two independent propagation modules; one to propagate the pulse train from the transmitter to the target, and one to propagate the pulse train from the target to the receiver. We have currently implemented a free space propagation model [5], but are implementing the WaveTrain [6] atmospheric propagation model for scenarios within the atmosphere. The WaveTrain model essentially passes the far field amplitude distribution through a series of phase screens. Additional propagation effects such as attenuation may be added using standard codes such as ModTran.

2.4. Target Modeling

The target model module allows us to define a target shape, including materials and surface properties, and its dynamics at any point in time.

Target shape may be selected from some basic geometric models such as cones or spheres. More complex objects can be specified using a CAD modeling program. The CAD model approach allows the use of arbitrary shaped objects with arbitrary mass distribution and surface material properties. Target location and orientation at any time are uniquely specified by six parameters corresponding to the 6 Degrees Of Freedom (6DOF). These six parameters are three spatial location parameters (x,y,z), and three Euler angles for orientation (yaw, pitch, roll) [7].

Different target propagators can be used, depending on the application. For our current work, we use an exo-atmospheric ballistic propagator, requiring initial conditions consisting of position and orientation, and the rates of each (6DOF and 6DOF rates). For the basic geometric shapes, the target dynamics are characterized by the tensor of moments of inertia (a 3x3 matrix) and are governed by the system of Euler and Poisson equations dealing with angular rates. The aspect angle, the coning angle, and the precession rate are specified in initial conditions. The center of mass can be calculated from a mass density function, but the default is the homogeneous target.

Target surface optical properties are characterized by a five parameter Bi-directional Reflectance Distribution Function (BRDF) derived from empirical data by Yoder [8] (note that since this is a modular simulation, alternative BRDF models can be easily substituted). The Yoder BRDF includes diffuse, retro-reflective, and glint reflectivity. The coefficient ρ_d characterizes the diffuse component, ρ_{rr} the retro-reflective component, and ρ_g , p , and q the glint component. These coefficients are dependent on the wavelength. For each scatterer:

$$BRDF = \frac{\rho_d}{\pi} \cos^2(\alpha) e^{i\theta} + \frac{\rho_{rr}}{2\pi} \cos(\alpha) + \frac{\rho_g}{\pi^2} e^{-p\alpha^q} \quad (2)$$

where α is the angle between the LOS and the normal vector to the surface of the scatterer. The $e^{i\theta}$ factor in the diffuse term represents a random phase term resulting from surface roughness. This term is the origin of target speckle.

In order to generate a Range Resolved Doppler Image (RRDI), we use four intermediate “images” or target maps (figure 4). Each of these “images” is a 2 dimensional map of some value as a function of cross range position. One image is a map of relative range to each target surface element versus position, one is a map of velocity in the Line Of Sight (LOS) direction (range rate), one is a map of the cosine of the angle between the a vector normal to the surface element and the LOS vector, and the final one is a map of surface material properties. The first three of these are floating point maps, while the surface material map is just an integer index to a table of material properties, which are the BRDF coefficients.

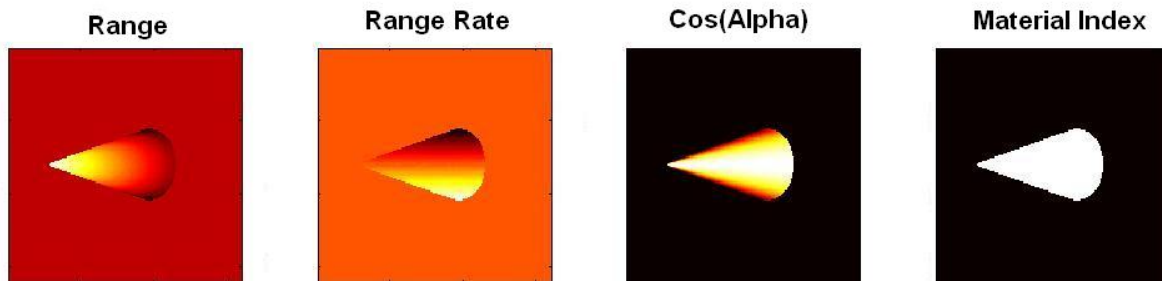


Figure 4. Four input “images” describing target.

The “images” are generated from the target model, its 6DOF values, and their derivatives. These images are parallel projections of the visible (and illuminated) part of target in the direction of LOS (also called the target cross-sections). Clearly, not all surface elements are visible to the receiver. The visibility is coded in the third array: if the cosine of the angle between normal and LOS is positive, then the scattering element is visible; if there are several scattering elements in the same LOS to the receiver, then the one that is closest to the receiver determines the visibility (this is known as the Z-buffer technique [9]).

2.5. Target-Beam Interaction

The target can be considered to be composed of a number of scattering elements (scatterers). Each scatterer is characterized by its area, the normal vector, the range and velocity (both measured in the direction of LOS), and the reflectivity (BRDF) of its surface material. The train of pulses (macro-pulse) is like a space-time coordinate system, which allows us to measure the range and velocity of scatterers in the direction of LOS. However, the identity of individual scatterers will be lost at the receiver. Instead we will get them in groups having near-identical (range, velocity) parameters. These groups are called range-Doppler bins (pixels). The range value is proportional to the time delay of the pulses: clearly, the later it arrives at the receiver, the farther it is from it. Similarly, the velocity of a scatterer (in direction of LOS) is directly proportional to the Doppler frequency shift of the reflected wave. Hence, the range-velocity diagram of target is identical, up to a linear scaling factor, to the time-frequency diagram.

The basic RRD image formation begins by generating a “pristine” Angle-Angle image. This uses the cosine image and the BRDF parameters from the material properties image to obtain the target reflective properties. A pristine range-

Doppler image is created from the Angle-Angle image and does not require any transmission of the modulated E-field. The pristine range-Doppler image is a specific 2D histogram (Lebesgue-Stieltjes integral in continuous modeling) built from the range matrix R, the velocity (range rate) matrix V and the Angle-Angle image A. The pristine range-Doppler image (RDI) is an MxN matrix, where M is the number of range bins and N is the number of velocity bins, both defined in figure 3. The value of RDI(r_1, c_1) of this matrix is the sum of all A(r_2, c_2) such that R(r_2, c_2) is the r_1 -multiple of the range step size, and V(r_2, c_2) is the c_1 -multiple of the velocity step size. Again, the step sizes are defined in figure 3. Clearly, we round the corresponding values in order to have the integer indices r_1 and c_1 .

The fundamental equations relating time delay to range and frequency shift to Line Of Sight (LOS) velocity are:

$$\begin{aligned} \text{Time Delay} &= \frac{2 * \text{range}}{c} \\ \text{Frequency Shift} &= \frac{2 * \text{velocity}}{\lambda} \end{aligned} \quad (3)$$

If the range extent is from 1 km to 1000 km, then the time delay is from 6.7 μ s to 6.7 ms. If the velocity extent is from 10 m/s to 10 km/s and $\lambda = 1.06 \mu\text{m}$, then the Doppler frequency extent is from 18.8 MHz to 18.8 GHz.

The material reflectance and angle between normal vector and LOS act to reduce the amount of return power. A perfect mirror perpendicular to LOS would return 100% of the incident wave. Rough or matte surface which is not perpendicular to the LOS will return less than 100%. The BRDF (equation 2) is used to compute the amount of reflected light. Since the target is illuminated by a non-homogeneous cone of light, we also take into account the transmitter illumination pattern.

The target-beam interaction results in four types of changes that convert the incident wave to reflected wave: the time delay with the information about the range, the amplitude modulation (angles and BRDF) which carries the information about the material reflectivity and surface shape, and the frequency modulation, which carries the information about the velocity (for each scatterer). Surface roughness of diffuse targets results in an additional random phase modulation which ultimately results in target speckle.

The Angle-Angle image is equivalent to the parallel projection of the visible elements of the target to a plane perpendicular to the line of sight and located in front of the target. The visibility of target elements is determined by the values of cosine between the normal and the line of sight. The intensity of pixels at the Angle-Angle image is determined by the (positive) value of the cosine and BRDF. The diffuse component of BRDF can be included with or without the random phases.

The transmitted signal (E-field amplitude) is $E(t) = E_0(t)e^{i2\pi ft}$, where $f = c/\lambda$ is the carrier frequency and $E_0(t)$ is the amplitude modulation of the pulse trains (macro-pulses). Then for k^{th} scatterer having the range r_k in LOS, the velocity v_k in LOS and the BRDF reflectivity coefficient b_k , the time shift is $2r_k/c$, the frequency shift is $2v_k/\lambda$, and the amplitude of the reflected wave (after some algebra) is

$$E_k(t) = b_k E_0 \left(t - \frac{2r_k}{c} \right) e^{i2\pi \frac{2r_k}{\lambda}} e^{i2\pi \frac{2v_k}{\lambda} t} e^{i2\pi ft} \quad (4)$$

In the above formula, the second term is the time-shifted transmitted signal, the third term represents the range phase shift and the fourth term represents the Doppler frequency shift. A diffuse scattering random phase shift is contained in b_k in the first term. The formula for entire target is the single-index summation of the above terms. When we build the signal from 4 matrices, then the summation is over the rows and columns (the double integral in the continuous model).

2.6. Receiver

The receiver segment models the detection process in which photons are converted first to photo-electrons and ultimately to digital counts and then into an RRD image. While a photon counting direct detection model is currently under development, we describe here our existing heterodyne detection module.

In a heterodyne detection process, the incoming complex valued signal E-field (E_S) is coherently mixed with a local oscillator E-field (E_{LO} from a local source laser). The resulting E-field now impinges on a conventional single pixel square law detector, which samples the intensity of the resulting E-field [2, 10]:

$$I(t) = \left| E_{LO} e^{i\omega_{LO}t} + E_S(t) e^{i\omega_S t} \right|^2 = E_{LO}^2 + E_S^2(t) + 2E_{LO} E_S(t) \cos((\omega_S - \omega_{LO})t) \quad (5)$$

The local oscillator intensity term is assumed constant and the signal only intensity term is assumed small, so that the target information is carried predominantly on the local oscillator times signal cross term (the heterodyne term). The local oscillator amplitude, E_{LO} is constant, so what we observe at any given intermediate frequency ($\omega_S - \omega_{LO}$) is proportional to the target signal amplitude, not the signal power (even though we are of course detecting optical power). This is important when discussing signal statistics in section 3.

The noise sources resulting from this process include background scattered light, local oscillator and signal induced shot noise, detector dark current, and Johnson noise produced by the amplifier. Since the local oscillator can be made much stronger than the signal, this should dominate signal, detector, and amplifier noise contributions, leaving only local oscillator and background noise sources. In general, background light will not be coherent with the local oscillator and hence will have a negligible contribution. The optical system has an optical throughput efficiency and a detection quantum efficiency, describing how many incident photons reach the detector and how many of those are converted to photo-electrons. Finally, the heterodyne efficiency accounts for the wavefront mismatch of the local oscillator and signal beams at the detector (including polarization and frequency stability), and the fraction of the signal collected by the detector (the signal blur spot is typically larger than the detector pixel).

The simulation determines how much of the return radiation is captured by the optical system (based on the receiver aperture diameter and range from target), and how much passes through the optical system to the detector (optical efficiency). The heterodyne process is modeled with local oscillator noise and a heterodyne efficiency factor. Next, a detector quantum efficiency is applied and detector noise (usually negligible) is added. The resulting photo-current is sampled and digitized into digital counts.

Recall that the out-going pulses of width T_p were spaced T_s apart. We sample the return signal in blocks of length T_s . The correct Nyquist spacing for individual samples is $T_p/2$ so that we obtain $2T_s/T_p$ samples per interval (although the exact sample rate is an adjustable parameter). We form a 2-dimensional array in which each row contains the samples for one time interval, T_s . Each row in this matrix now corresponds to a separate out-going pulse, and each sample across the rows corresponds to a time delay which in turn can be scaled to a range difference. The values in the array are proportional to the signal amplitude, E_S . We refer to this initial image as the pulse sequence image. By taking a one dimensional Fourier transform along each column, we obtain a time-frequency array which is then scaled into the final Range-Velocity image.

2.7. Signal Processing and Image Processing

The initial RRD image can be filtered with a variety of time-frequency techniques (corresponding to the range and velocity dimensions of the RRDI) to reduce noise in the image and improve the subsequent target feature extraction. The purpose of this filtering is to separate signal from the noise. In these transforms the target (encoded as 2D Probability Distribution Function - PDF) appears as a 2D object embedded in noise. The noise that surrounds the target in the 2D representation can be separated easier than in a 1D mixture of the signal and noise.

The toolbox here is rather large and not yet fully explored. We have implemented several Short-Time Fourier Transforms [4]; the most important these being the sliding Gaussian window (Gabor transform), and Short-Time Cosine Transform. In addition we have implemented the pseudo-Wigner and Wigner-Ville transforms – members of the general Cohen class transforms, and the Empirical Distribution Modes (EMD). We have also implemented several wavelet transforms, including the Mallat, Morlet, and Meyer transforms. A partial list is shown in figure 5.

The image processing segment consists of three steps. First is the background noise estimation, then the background noise subtraction, and finally, the image cleanup to remove the outliers and spikes using majority rule and Neyman-Pearson segmentation.

Short-Time Fourier Transform ¹¹	$F(\omega, \tau) = \frac{1}{\sqrt{2\pi}} \int_{-\infty}^{\infty} f(t)w(t-\tau)e^{-i\omega t} dt$
Pseudo-Wigner Transform ¹²	$PW(\omega, t) = \int_{-\infty}^{\infty} f\left(t+\frac{\tau}{2}\right)f^*\left(t-\frac{\tau}{2}\right)h\left(\frac{\tau}{2}\right)e^{-i\omega\tau} d\tau$
Wigner-Ville Transform ¹²	$WV(\omega, t) = \int_{-\infty}^{\infty} f\left(t-\frac{1}{2}\tau\right)f^*\left(t+\frac{1}{2}\tau\right)e^{-i\omega\tau} d\tau$
Morlett Wavelet Transform ¹³	$MoW(a, b) = \frac{1}{\sqrt{a}} \int_{-\infty}^{\infty} f(t)\psi\left(\frac{t-b}{a}\right)dt, \quad \psi(t) = e^{-2\pi i t} e^{-\frac{t^2}{2}}, a > 0$

Figure 5. Various signal processing transforms

This signal and image processing segment is driven by strict quality control via signal-to-noise ratios, since its purpose is to provide quality input to the feature extraction segment. However, with too aggressive denoising the target image may lose width or height, fine details, connections between parts, etc.

Multiple RRD images can now be summed together to form a single Post Detection Integration (PDI) image. This is an incoherent sum (since we have lost phase information in the detection process). This process tends to average noise, in particular phase noise resulting in speckle, while adding signal.

2.8. Feature Extraction

Instantaneous features are extracted from each individual RRD image, while temporal features are extracted from a time series of instantaneous feature values collected during the observation of the target. A few basic features can be extracted from almost all RRD images. These are the range extent of the target, the Doppler width (or spread), the total number of pixels, and the total energy returned from the target. For simple geometric shaped targets, we can extract some general temporal features related to each of the instantaneous parameters. Each of the features may be modulated in time. Thus we can extract the period of modulation, the amplitude of modulation, and the phase. With complex shaped objects, the modulation may have multiple frequency components. We have implemented only generic feature extraction algorithms for the features just described. More complex algorithms may be desired for specific applications. A detailed discussion of these algorithms is beyond the scope of the current paper. Instead we provide a brief overview of our approach.

In case of an axial symmetrical target, such as a sphere or cone, for each bin with velocity v there is a bin with velocity $-v$. Thus we can estimate the location of the zero velocity bin. If target has a conical shape, then we can estimate the *tip velocity*, which is related to target spin and precession.

In the case of a conical-shaped target we use the method of moments to estimate the edges of target image in RDI. This method uses a least squares approximation of edges by lines using the property that each target row (consisting of bins with the same range) has nearly uniform distribution. So, the “shape” features mentioned above are represented by single triangle, where the base length is the *base velocity spread*, the height is the *projected length*, and the top vertex of the triangle represents the *tip velocity* (relative to the center of the triangle base). We compare the feature values extracted from the noisy RRDI to the feature values extracted from the pristine RRDI.

The feature values extracted from a sequence of range-Doppler images represents a multivariate time series. Unfortunately, some channels usually have very low quality of data. It turns out, that the temporal features have a periodic nature, thus we need to identify and extract certain frequencies from the spectra of these time series. So, we try to identify the *dominant frequency* in the temporal feature data (in some channel). We developed an algorithm which uses several competing principles in a search for the dominant frequency and selects the best fitting frequency. These principles include spectral analysis, autocorrelation, and least squares approximation. Actually, we identify several significant frequencies in the spectrum of a feature time series; these frequencies are ordered by decreasing magnitude of their presence in the spectrum. It turns out that the first dominant frequency corresponds to precession, and after skipping through a few harmonics of the precession, we may find the spin frequency.

One important step in the verification of the simulation was to ensure that the dynamic parameters specified in the target modeling segment of the simulation would coincide (or be sufficiently close to) those extracted in this temporal extraction segment.

The spatial and temporal (dynamic) characteristics of various targets are now compared to data either imported or collected from multiple runs of the simulation. The goal is to classify (discriminate) targets according to some proximity rules and “feature merging” rules. Here we use several approaches: the kNN classification approach with suitable distance (proximity) functions and the Dempster-Shafer theory of evidence for combining (merging) multiple data having yet inconclusive partial evidence into the decisive summary evidence [14]. The efficiency of this segment still has to be tested with large data sets collected from experiments.

3. VALIDATION

3.1. Overview

We performed three types of test to validate performance of the simulation: 1) Compared target noise statistics obtained from our simulation imagery with theoretically predicted statistics, 2) Generated both pristine and noisy imagery and then compared extracted target features with the input target parameters, and 3) Performed comparisons with laboratory test data using real ladar devices and targets.

The target selected for the test was a homogeneous standard circular cone with a uniform Lambertian surface. The cone was set to have a fixed spin rate about its center of mass and no precession rate. These settings combined with the aspect angle generated the four target mappings corresponding to the target ranges from sensor in line of sight, the target velocities in line of sight, the cosine of the surface normal to the line of sight, and a material index of the target.

The transmitter and receiver parameters were selected to be similar to laser radar resources and laboratory configurations. The transmitter was assumed to have a Gaussian spatial beam profile composed of pulses with Gaussian temporal profiles, with the pulse spacing significant enough to remove overlap of pulses on the returned signal. The transmitted beam profile shape used was a volume-normalized Airy-like distribution dependent on the transmitter diameter and the beam divergence angle in the far-field. The simulated illumination center (aimpoint) selected in the testing procedure was the center of mass on the cone. The receiver was assumed to have a circular aperture of fixed size significant enough (generally, no more than a factor of ten greater than the transmitter aperture diameter) to receive the returned signal from a variety of reasonable distances similar to those found in the laser radar literature.

In the signal and image processing stage of the simulation, a Gaussian distributed random noise is added to the simulated returned signal to account for the Local Oscillator (LO) shot noise. The noise power is determined from the local oscillator power on the detector pixel. The LO power is adjusted to ensure this is the dominant noise term. The simulated time-series signal was processed using a one dimensional fast Fourier transform to generate the frequency distribution of the signal. This frequency distribution was then formatted as the range resolved Doppler image. In addition, the simulation was set up to generate Post-Detection Integration (PDI) images. The PDI image is constructed by generating and summing a fixed number of Range-Doppler images. This number of range-Doppler images used to create a PDI image is an adjustable parameter in the simulation.

For the laboratory comparison, we are able to report that we performed a number of comparisons and obtained similar results with both the laboratory data and the simulation data.

Figure 6 shows an angle-angle image with the transmitted beam profile; essentially this image is the target cross-section mapping.

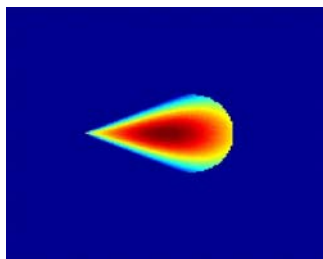


Figure 6. Angle-Angle image with transmitted beam profile.

3.2. Statistical Evaluation

We performed a comparison of the statistical noise distributions obtained from simulation imagery with theoretically predicted distributions (Osche) [15]. When the lidar illumination impinges on a diffuse surface, each separate surface element imparts a random phase on the electric field scattered from the surface element. This results from the fact that the surface is rough on the scale of a wavelength. When these E fields are summed at the detector, the random phases combine to produce constructive or destructive interference (speckle), so that the target signal amplitude and intensity have a statistical nature, which depends on the particular choice of random phases (each realization of the phases produces a different intensity). This type of diffuse target is known as a Swerling Type 1 target [16] and results in a Rayleigh probability distribution of amplitude (eq 6) and a negative exponential probability distribution of intensity (eq 7), where A is the observed signal amplitude, I is the observed signal intensity at any instant in time and n is the mean signal power. The parameter s is related to the mean signal power n, by $n = s\sqrt{\pi/2}$.

$$P(A) = \frac{A}{s^2} e^{-\frac{A^2}{2s^2}} = \frac{\pi A}{2n^2} e^{-\frac{\pi A^2}{4n^2}} \quad (6)$$

$$P(I) = \frac{1}{n} e^{-I/n} \quad (7)$$

Other types of statistics are produced for a specular (non-fluctuating) target. Recall that using heterodyne detection, we actually sample the signal amplitude. If we use the original pulse sequence image, we must square the individual pixel values in order to obtain an image which is proportional to the signal power. Figure 7 shows amplitude statistics of a pulse sequence image obtained from the simulation (left) and the intensity statistics obtained by squaring the pulse sequence image pixel values (right). The left hand figure is overlaid with a theoretical Rayleigh distribution while the right hand figure is overlaid with a negative exponential distribution, both of which are generated using eqn 6 and 7.

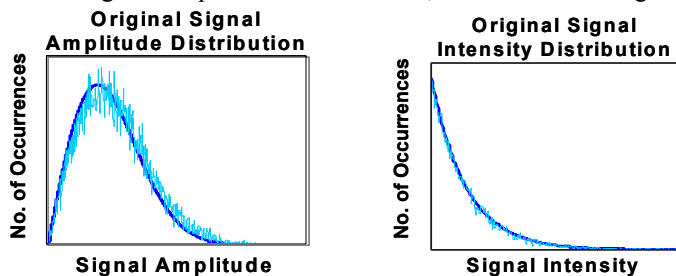


Figure 7. Pulse sequence image Amplitude (left) and Intensity (right) distributions for target signal obtained from the simulation compared with a Rayleigh and negative exponential distribution

The RRD image is obtained by taking one dimensional Fourier transforms on each column of the (amplitude) pulse sequence image. The distribution of this RRD image is also a Rayleigh distribution. Multiple RRD images may be summed to form a PDI image. The statistics of this image, by the Central Limit Theorem, will tend toward a Gaussian distribution. We generated a number of RRD images and compared their distributions with that of a Rayleigh distribution (figure 8). We also formed a 7 frame PDI which as predicted exhibited a Gaussian distribution. It should be noted that the statistics for the signal originate solely from the addition of the target E fields; the functional form is not input. The noise statistical distribution is not used in the code, but it can be seen that the sum of signal plus noise agrees with the theoretical.

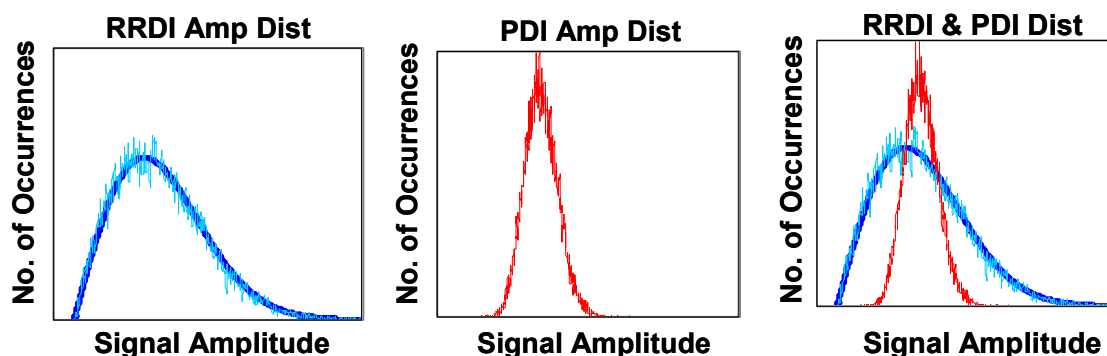


Figure 8. Sample distributions for both individual and 7 frame PDI Range Doppler images.

3.3. Feature Extraction Test

We used a spinning cone of known length, diameter and spin rate (and hence base velocity spread) to generate both individual RRD images, and PDI images. We generated both noise-free image sets and also image sets with varying levels of receiver noise (figure 9).

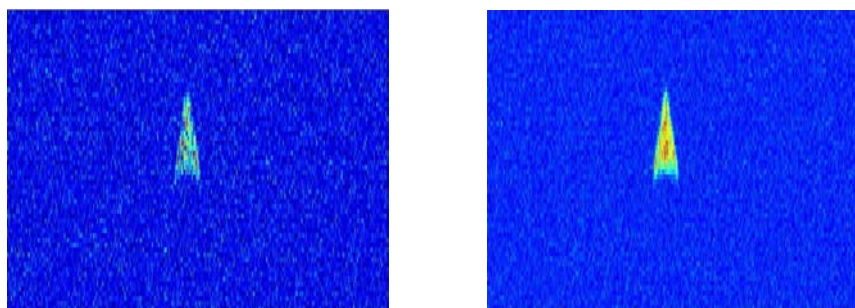


Figure 9. Imagery with receiver noise: Single image (left) and PDI image (right)

The feature extraction part of the simulation constructs a bounded region around the target; the shape of this bounded region is determined by the target shape. In the test case the target was a cone, therefore the best bounding region for the range-Doppler image has a triangular shape. This triangular region was generated using a least squares approximation after the image has been filtered. The feature extraction algorithm produces a series of five images showing the steps in generating the bounded region (figure 10). The first image produced is the actual range-Doppler image. The second image is a filtered version of the original, using a background statistics filter on the intensity of the image. The third image is a binary version of the filtered second image; this image is used to calculate the least squares approximation to the edges of the target. The fourth image generated is the binary range-Doppler image with the feature extraction framework overlaid onto the image. The final image is the feature extraction framework overlaid onto the original range-Doppler image.

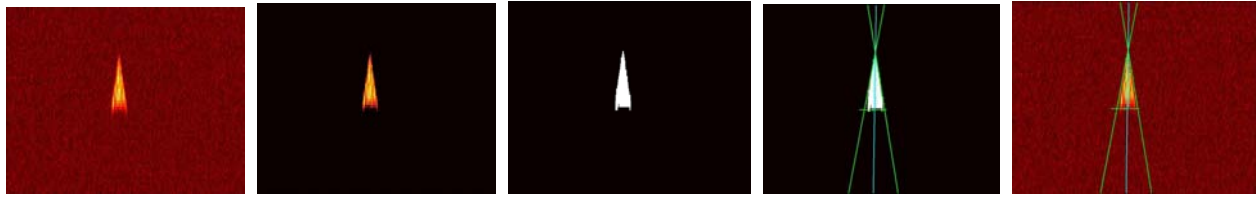


Figure 10. Feature extraction from noisy imagery

In addition to the images generated, this part of the simulation also reports the tip velocity, range extent, base velocity span, and signal-to-noise ratio (SNR). The values are reported in pixel units (as opposed to engineering units). The features extracted from the non-noisy images are used to confirm the amount of target loss in the filtering process.

The non-noisy images show a best case scenario for the system. Therefore the comparison of the features from the non-noisy and the noisy images shows the amount of loss due to the additive Gaussian noise from the local oscillator shot noise on the receiver. The following chart shows the primary features: base velocity spread, range span, and tip velocities for the non-noisy and noisy range-Doppler images. The numbers on this chart show that the features extracted by the simulation algorithms are nearly identical for the base velocity span and the range span. The tip velocity feature is the most susceptible to larger variations in the features extracted between noisy and non-noisy images are due to the process of filtering the noise from each image.

Non-Noisy Images	Tip Velocity	Base Velocity Span	Range Span
RD # 1	0.41	42.54	20.85
RD # 2	-0.45	42.39	20.62
RD # 3	0.72	43.64	20.17
RD # 4	1.14	47.16	19.43
RD # 5	0.11	51.23	19.22
RD # 6	-2.35	42.17	20.60
RD # 7	1.06	44.25	20.74
PDI	-0.69	48.91	21.94

Noisy Images	Tip Velocity	Base Velocity Span	Range Span
RD # 1	6.25	33.92	20.17
RD # 2	-1.79	39.68	16.78
RD # 3	3.52	36.98	19.97
RD # 4	2.52	44.76	17.62
RD # 5	3.78	41.01	21.04
RD # 6	-1.25	37.61	18.50
RD # 7	-0.81	45.41	18.54
PDI	1.76	44.47	19.23

Figure 11. Feature values extracted from noisy and non-noisy imagery.

The non-noisy feature values were compared with the known target truth values. The target tip velocity was 0. The non-noisy image base velocity span was within 3% of the target truth value and the range span was with 8% of the target truth value.

Carrier to Noise Ratio (CNR) is a useful metric when calculating detection probabilities and quantifying radar performance. However, when performing feature extraction on a RRD image, Signal to Noise Ratio (SNR) is a better metric. In radar applications, the CNR is defined [10] as signal power divided by noise power, while SNR is defined signal power divided by noise variance. In image processing, we typically work with the square root of these quantities so that we are working with the statistics of pixel values instead of squared pixel values. The noise mean and standard deviation are estimated using regions of the RRD image which are known not to contain the target. The target mean value is estimated as the mean value of the signal in the target region of the image, with the noise mean value subtracted. Thus if μ_N is the noise mean value, σ_N is the standard deviation of the noise, and μ_{TN} is the mean value of the target plus noise:

$$CNR = \frac{\mu_{TN} - \mu_N}{\mu_N} \quad (8)$$

$$SNR = \frac{\mu_{TN} - \mu_N}{\sigma_N} \quad (9)$$

When several images are averaged (PDI), the CNR remains constant (because the average signal and noise remain constant), but the SNR increases (because the noise variance is divided by the number of images averaged). We examined the Carrier-to-Noise ratio and the Signal-to-Noise ratio which showed the noise mean and variance remaining relatively constant between range-Doppler images in a series (figure 12). In addition, the PDI image made from seven range-Doppler images showed that the noise variance was reduced by a factor of seven compared to an individual range-Doppler image. The CNR value remained relatively constant for each range-Doppler image and the PDI image whereas the SNR increased as expected, by the square root of seven.

	RD # 1	RD # 2	RD # 3	RD # 4	RD # 5	RD # 6	RD # 7	PDI
Noise Mean	0.418	0.417	0.415	0.416	0.418	0.418	0.418	0.416
Noise Variance	0.048	0.048	0.048	0.048	0.047	0.048	0.049	0.007
Signal + Noise Mean	1.62	1.41	1.57	1.55	1.41	1.44	1.38	1.37
CNR	2.88	2.38	2.78	2.73	2.37	2.44	2.30	2.29
SNR	5.49	4.53	5.27	5.18	4.58	4.66	4.35	11.40

Figure 12. CNR and SNR for single RRD images and for 7 frame PDI image

4. SUMMARY

We have developed a modular lidar simulation which allows us to model various lidar transmitter properties, target interactions, beam propagation, and receiver properties. We have also modeled receiver signal processing and feature extraction algorithms. The modular nature of the simulation allows us to select various different simulations (e.g. free space or atmospheric propagation, or various signal processing algorithms). We have quantitatively validated the simulation imagery against theoretically predicted noise distributions and the entire simulation including feature extraction, against known input target parameters. We have also qualitatively compared results of the simulation with laboratory tests using real physical devices and targets.

The result is that we have a simulation in which we have high confidence and which we can use to tune various lidar device parameters and algorithms for specific applications. Furthermore, we can expand the existing simulation to support future requirements and are in fact actively engaged in adding additional beam propagation and receiver module options.

ACKNOWLEDGMENTS

The authors would like to acknowledge the help of Ralph Pringle for his ideas in the basic lidar algorithm simulations and Matt Drago for his assistance with radiometry and receiver issues.

REFERENCES

1. Merrill I. Skolnik, "Radar Handbook", McGraw-Hill, Boston, MA., 1990.
2. Gary W. Kamerman, "Laser Radar", The Infrared Handbook Vol 6, Ch 1, (Joseph W. Accetta, David L. Shumaker, Exec. Editors), ERIM & SPIE Optical Engineering Press, Bellingham, WA, 1993.
3. Albert V. Jelalian, "Laser Radar Systems", Artech House, Boston-London 1992.
4. Douglas G. Youmans, "Theoretical and Monte Carlo Analyses of the Range-Doppler Imaging Capabilities of Mode-locked CO₂ Ladars", Proc. SPIE, **2702**, pp 40-51.

5. Joseph W. Goodman, "Fourier Optics", McGraw-Hill, Boston, Mass., 1996. pp 63-89.
6. Steven Coy, "WaveTrain: A User-Friendly Wave Optics Propagation Code", Proc SPIE, **3706**, Aug 1999.
7. Herbert Goldstein, "Classical Mechanics", Addison-Wesley, Reading, Mass., 1980. pp 132-187, 606-610.
8. M. John Yoder, "Comparison of BRDFs, missile cross-sections and airborne laser radar ranges at wavelength of 10.6, 1.06 and 0.6 μm ", IRIS Specialty Group on Active Systems, Naval Postgraduate School, Monterey, CA, 24-26 February 1999.
9. James D. Foley, Andries van Dam, Steven K. Feiner, John F. Hughes, "Computer Graphics: Principles and Practice", Addison-Wesley, New York, 1992. pp 668.
10. J. H. Shapiro, B. A. Capron, and R. C. Harney, "Imaging and target detection with a heterodyne-reception optical radar", Applied Optics, **20** (19), 1 October 1981, pp. 3292-3313.
11. Victor C. Chen and Hao Ling, "Time-frequency transforms for radar imaging and signal analysis", Artech House, Boston – London, 2002.
12. Paulo Gonçalves, Richard G. Baraniuk, "Pseudo Affine Wigner Distributions: Definition and Kernel Formulation", IEEE Trans Signal Processing, **46** (6), 1998. pp 1505–1516.
13. Stéphane Mallat, "A Wavelet Tour of Signal Processing", Academic Press, San Diego, 1998. pp 80, 246, 255.
14. Edward Waltz, James Llinas, "Multi-Sensor Data Fusion", Artech House, Boston, MA, 1990.
15. Gregory Osche, "Optical Detection Theory for Laser Applications", John Wiley and Sons, Hoboken, 2002. pp 363-381.
16. P. Swerling, "Probability of Detection for Fluctuating Targets", IRE Trans. IT-6, April 1960. pp 269-308.